Liquid Metal Corrosion of 316L Stainless Steel, 410 Stainless Steel, and 1015 Carbon Steel in a Molten Zinc Bath

JING XU, MARK A. BRIGHT, XINGBO LIU, and EVER BARBERO

Corrosion tests of 1015 low-carbon steel and two stainless steels (410 and 316L) were conducted in a pure zinc bath (99.98 wt pct Zn) in order to better understand the reaction mechanisms that occur during the degradation of submerged hardware at industrial general (batch) galvanizing operations. Through this testing, it was found that, in general, 316L stainless steel showed the best dissolution resistance among these three alloys, while 1015 carbon steel provided a lower solubility than 410 stainless steel. Investigating the failure mechanisms, both metallurgical composition and lattice structure played important roles in the molten metal corrosion behaviors of these alloys. High contents of nickel combined with the influence of chromium improved the resistance to molten zinc corrosion. Moreover, a face-centered-cubic (fcc) structure was more corrosion resistant than body-centered-cubic (bcc) possibly due to the compactness of the atomic structure. Analogously, the body-centered-tetragonal (bct) martensite lattice structure possessed enhanced susceptibility to zinc corrosion as a result of the greater atomic spacing and high strain energy. Finally, an increased bath temperature played an important role in molten metal corrosion by accelerating the dissolution process and changing the nature of intermetallic layers.

I. INTRODUCTION

HOT dip zinc-coated steel production has increased dramatically over the past decade due to its relative economic benefits over other corrosion-resistant materials. As a result of this increased demand, the need for greater manufacturing efficiency in the galvanizing process has also gained prominence. Numerous projects have investigated the molten metal corrosion aspects of materials and designs used for the submerged pot rolls and other hardware of continuous sheet galvanizing operations.[1,2] The degradation and frequent failure of these structures results in significant production downtime and leads to high maintenance costs due to extensive repair and replacement.[3]

In order to prolong the service life of these rolls, many studies have attempted to obtain a better understanding of the corrosion behavior of the hardware materials in a variety of compositional coating baths.[4–8] However, the test conditions and focus of each of the projects have been quite broad, encompassing ferrous alloys, cobalt alloys, coatings, and weld materials. Concurrently, extensive research has been executed to define the equilibrium phase diagrams relevant to galvanizing applications. A standard Zn-Al-Fe phase diagram has only recently been accepted,[9] while other more advanced zinc phase diagrams involving Cr, Ni, Co,

and others are currently being formulated.[10–13] However, with this array of research focused on materials for continuous galvanizing pot rolls, minimal effort has been directed toward understanding the molten metal reactions of hardware and containment kettles employed in general (batch) galvanizing,[14,15] which uses zinc possessing very low levels of aluminum and, hence, vastly different corrosion properties.[16]

In the current research effort, molten metal corrosion tests of three ferrous alloys (1015 low-carbon steel, 410 martensitic stainless steel, and 316L austenitic stainless steel) were conducted in pure zinc (99.99 wt pct Zn) to obtain a better understanding of the solubility of structural materials in a typical general (batch) galvanizing environment. The tasks entailed exploring the dissolution and corrosion kinetics of iron in molten zinc by observing the nature and rate of the corrosion attack and the interfacial reactions between the tested hardware materials and liquid zinc. The effect of the chromium content in the substrate materials, as well as the intrinsic phase differences therein, was also reviewed. The experimental results from this study not only enrich the knowledge pool of liquid-metal corrosion, but also provide solid clues to the effective selection of submerged hardware materials and the prediction of corresponding operating parameters, such as the maintenance frequency and the service life estimation.

JING XU, Graduate Research Assistant, XINGBO LIU, Assistant Professor, and EVER BARBERO, Professor, are with the Mechanical & Aerospace Engineering Department, West Virginia University, Morgantown, WV 26506. Contact e-mail: Xingbo.liu@mail.wvu.edu MARK A. BRIGHT, Technology Manager, is with the Metaullics Systems (Division of Pyrotek Incorporated), Solon, OH 44139.
Manuscript submitted February 7, 2007.
Article published online September 20, 2007.

II. EXPERIMENTAL SETUP

A. Materials

Three types of steels (316L austenitic stainless steel, 410 martensitic stainless steel, and 1015 ferritic carbon

Table I. Composition of Three Types of Steels (Weight Percent)

Materials	C	Si	Mn	S	P	Cr	Ni	Mo	Cu	N	Fe
316L ss	0.012	0.40	1.39	0.029	0.024	17.55	10.74	2.05	0.257	0.0512	67.497
410 ss	0.141	0.19	0.46	0.005	0.009	11.96	0.380	—	—	0.0658	86.789
1015 cs	0.157	0.17	0.50	0.029	0.009	—	—	—	0.343	0.0145	98.590

Table II. Matrix of Corrosion Testing Parameters

Immersion Specimen Materials	Testing Condition: Temperature (°C)–Time (Days)
1015 low-carbon steel	465 °C–14 days; 500 °C–8 days; 520 °C–4 days
410 ss	465 °C–17 days; 500 °C–7 days; 520 °C–4.5 days
316L ss	500 °C–6 days; 520 °C–12 days

steel; Table I) containing variable amounts of chromium, nickel, and molybdenum were considered for this investigation. Each material was cold rolled and annealed prior to machining test samples (15.9-mm diameter by 50.8-mm length). Dimensions and weights of the specimens were then recorded after pickling, degreasing, and cleaning in dilute HCl, acetone, and alcohol, successively.

B. Corrosion Testing

For each corrosion immersion test, a 41-kg bath of pure zinc with the starting composition (wt pct) 99.98 Zn, 0.011 Si, 0.003 Al, 0.002 Fe, and 0.002 Pb was heated to a set point of either 500 °C or 520 °C. A matrix of immersion materials and testing parameters (as shown in Table II) was chosen according to an estimated dissolution rate for each specimen material at the specified temperature. After immersion in the pure zinc bath for a given period of time, samples were pulled out one at a time at subsequent time intervals in order to determine the experimental corrosion degradation.

C. Characterization

Upon extraction from the liquid zinc, corrosion specimens were first pickled in a dilute (15 pct) HCl solution to remove the zinc adhering to the surface, and then ultrasonically degreased and cleaned in acetone and alcohol to ensure complete removal of the zinc. Subsequently, the weight and dimensions of each sample were measured in order to quantify the relative change in sample size so that corrosion rate determinations could be calculated. Meanwhile, several specimens from each test were maintained in their as-tested condition for the purpose of microstructural analysis. Each as-tested sample was cross-sectioned and mechanically polished then examined by optical microscopy and scanning electron microscopy (SEM). An integrated energy dispersive spectrometry (EDS) was employed to determine the concentration profiles and compositions of the phases within the reaction region between the ferrous substrate and residual zinc coating.

III. EXPERIMENTAL RESULTS

A. Corrosion Rate Identification

From the aforementioned testing, it was easily observed that all three ferrous alloys were attacked aggressively by the molten zinc. The corrosion behavior of these alloys was then characterized by three methods: weight loss, semi-instant corrosion rate, and average corrosion rate.

1. Weight loss

The calculation of weight loss directly describes the relative weight change of each specimen over the duration of the immersion time. As expected, it was observed that the weight of all three steel materials degraded progressively when immersed in molten zinc.

For 316L stainless and 1015 carbon steel, Figure 1(a) identifies a linear relationship of weight loss over time with 1015 carbon steel exhibiting a greater weight depletion than 316L at a comparative temperature (500 °C). The kinetic constant of the reaction process (K) can be determined from the slope of the plot representing the variation of the weight loss vs time. The K values associated with 1015 carbon steel were $K_{465\ °C} = 0.018$ g/h and $K_{500\ °C} = 0.407$ g/h at 465 °C and 500 °C, respectively, while 316L stainless exhibited the same K value at both 500 °C and 520 °C, $K_{316L} = 0.100$ g/h.

Determining the kinetic constant of 410 stainless steel was not as straightforward. As shown in Figure 1(b), each semiparabolic trend line possessed an initial high-corrosion region (K_I) then a subsequent region of greater stability (K_{II}). These K values for 410 stainless (outlined in Table III) suggest that the weight loss was influenced by not only the bath temperature but also the immersion time. Increasing the bath temperature accelerated the degradation of the 410 stainless with a prominent enhancement of the dissolution rate occurring between 465 °C and 500 °C. However, regardless of the temperature, each test eventually reached a domain of suppressed and stabilized weight loss (and, hence, lower values of K_{II}), identifying that the corrosion slows after a given initiation period (region I).

2. Semi-instant corrosion rate

The determination of the semi-instant corrosion rate takes into consideration the changing surface area of each sample over the given immersion period. However,
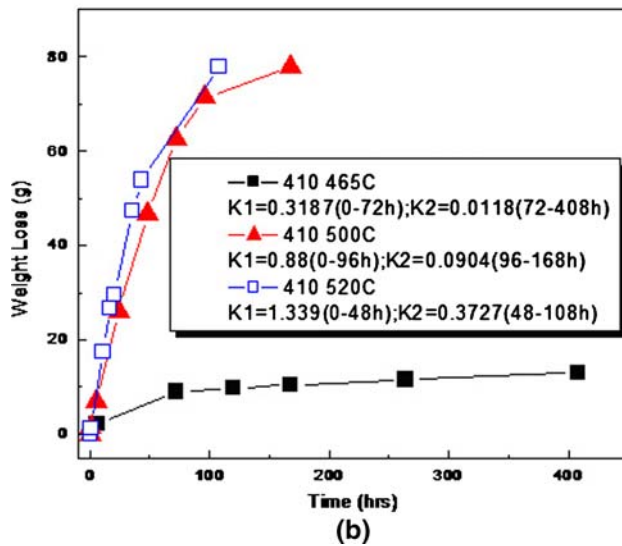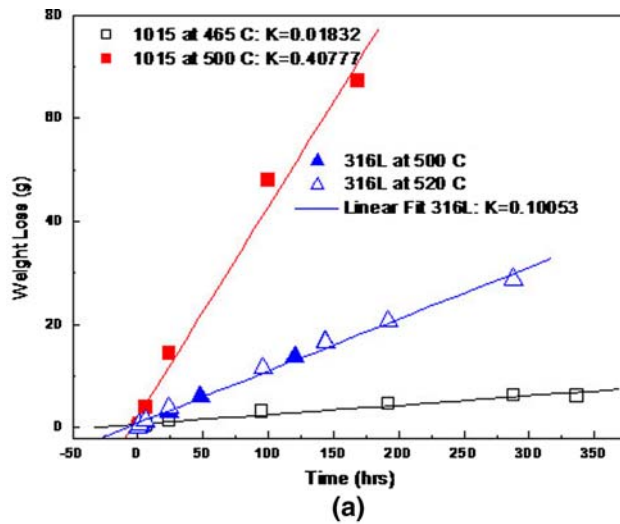
Fig. 1—Relationship between weight loss and time on steels exposed to pure zinc: (a) 1015 carbon steel and 316L stainless steel, and (b) 410 stainless steel.

Table III. Kinetic Constant (K) of the Weight Loss for 410 Stainless

Temperature (°C)	Kinetic Constant (K) g/h	
	Region I (K_I)	Region II (K_{II})
465	0.3187 (0 to 72 h)	0.0118 (72 to 408 h)
500	0.88 (0 to 96 h)	0.0904 (96 to 168 h)
520	1.339 (0 to 48 h)	0.3727 (48 to 108 h)

in order to compare the corrosion data of the experiments on different specimens, it was assumed that the three materials employed herein decayed based on uniform corrosion (*i.e.*, all the constituents in the substrate alloy dissolved into the bath at the same rate).[17] The formula used to calculate the semi-instant corrosion rate is shown as follows:

$$v = \frac{W_n - W_{(n-1)}}{\bar{A} \cdot t} \qquad [1]$$

where v represents the semi-instant corrosion speed (g/m² · h), W_n represents the specimen weight (g) at the starting time $t = 0$, $W_{(n-1)}$ represents the specimen weight (g) after immersion in the zinc for the experimental time t (hours), and $\bar{A}$ is the specimen average surface area (m²) at time $= t$.

Figures 2(a) through (c) profile the semi-instant corrosion rates (as compared to the aforementioned weight loss) of the three steels at 465 °C, 500 °C, and 520 °C, respectively. With the consideration for surface area calculated, 410 stainless exhibited the highest semi-instant corrosion rates among the materials tested regardless of testing condition. Meanwhile, 1015 carbon steel showed greater corrosion rates than 316L stainless steel.

3. Average corrosion rate

The concept of average corrosion rate defines the thickness loss of the material as projected over a full-year average, considering single-face zinc contact over the service period. The prerequisite of this technical definition is that the corrosion occurs uniformly from one exposed surface of the material, penetrating gradually into the substrate with only the depletion in wall thickness leading to the final weight loss. This rate calculation is relevant with respect to the degradation of the carbon steel lining of general (batch) galvanizing kettles, which hold a given volume of zinc for long time periods. The formula used to describe this process is shown as follows:

$$B = 8.76 \frac{v}{\rho} \qquad [2]$$

where B represents the average corrosion rate (mm/year), v the semi-instant corrosion rate (g/m² · h), and ρ the specimen density (g/cm³). Figure 3 shows the experimental relationship between average corrosion rate (squared) and time at different bath temperatures (465 °C, 500 °C, and 520 °C).

From the log-log plot of Figure 3, the time dependence of the average corrosion rate data shows that linearity occurs, but only after a transient period of about 24 hours. (In other words, the variation of the average corrosion rate squared *vs* time cannot be described by a straight line for durations less than 24 hours). In general, following the initial transient period, corrosion rates decelerated with the extension of the immersion time for all three steels, indicating that different kinetic regimes were involved during the immersion process. (Slopes of the linear region, representing the decay of the average corrosion rate, are summarized in Table IV.)

B. Metallurgical Morphology and Elemental Distribution Profile

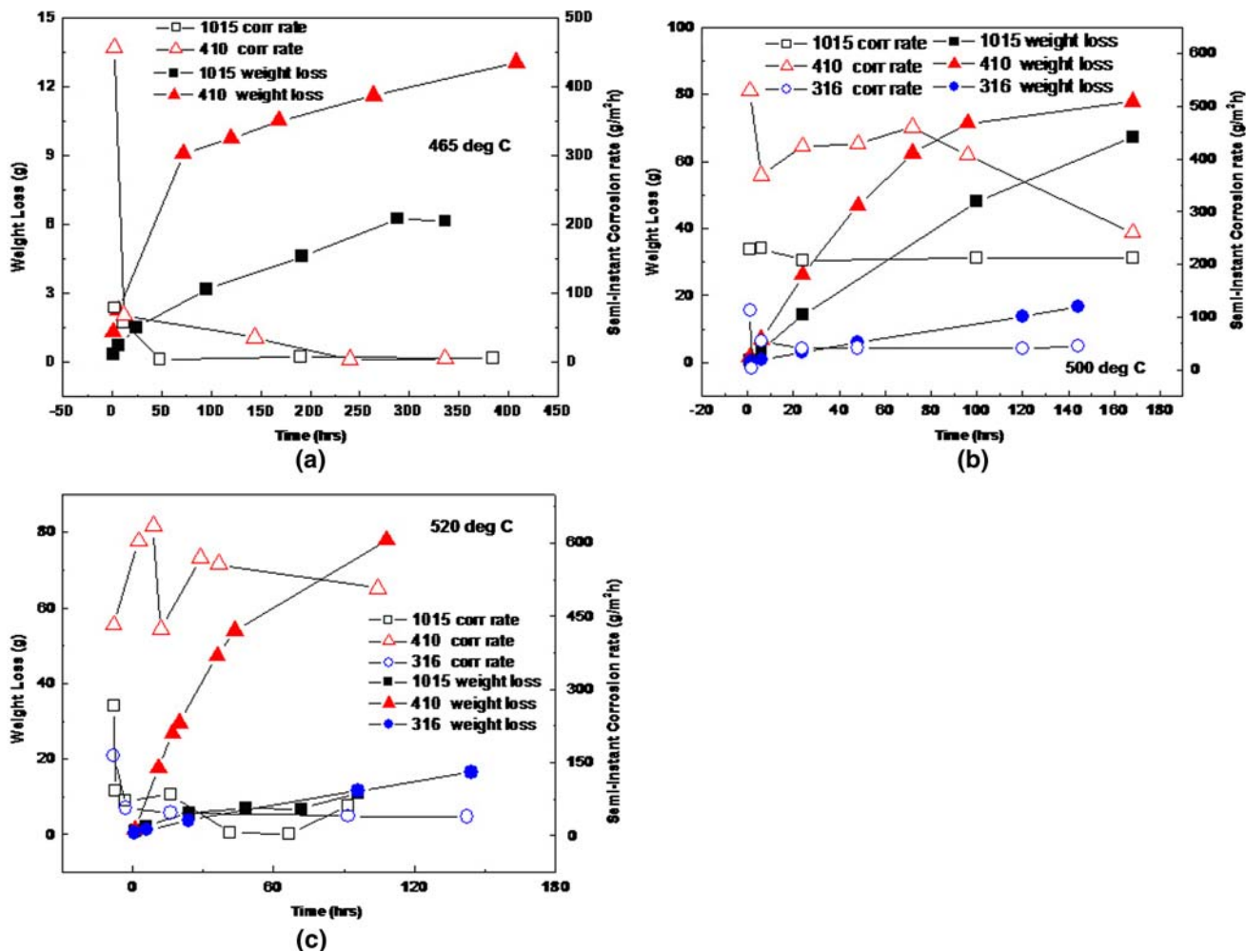With a determination of the physical deformation of the ferrous alloys after exposure to molten zinc, it was

Fig. 2—Weight loss and semi-instant corrosion speed of 1015, 410, and 316L steels exposed to pure zinc at (*a*) 465 °C, (*b*) 500 °C, and (*c*) 520 °C.

necessary to observe the metallurgical morphology of the specimens by optical microscopy and SEM and analyze the composition of the interfacial phases by means of EDS in order to better understand the reaction mechanisms interacting between the liquid zinc and substrate materials. As a result, micrographs displayed significant differentiation between each type of steel specimen when the immersion time was extended from a few hours to several hundred hours. Moreover, the zinc bath temperature had a strong influence on the cross-sectional structures and sublayer alignment.

1. *1015 carbon steel*

The 1015 low-carbon steel sample behaved in accordance with its documented behavior.[18,19] The typical intermetallic phases γ (Fe$_3$Zn$_{10}$), δ (FeZn$_7$), and ζ (FeZn$_{13}$) were identified using optical microscopy and were confirmed by SEM/EDS. As shown in the EDS profile of the 1015 carbon steel specimen immersed in liquid zinc for 24 hours at 520 °C (Figure 4(a)), a clear interface between the steel and solidified zinc was observed. From the steel face into the residual zinc region, the concentration of iron dropped tremendously in the first 30-μm affinity region, and then stabilized.

Figure 4(b) identifies the relative chemical composition near the affinity region (location 1) at the interface, hinting that it was predominantly γ phase. However, when this same material was tested in zinc at 500 °C for 168 hours, a notable difference in the morphology was observed. As labeled in Figure 5, the cross-sectional photomicrograph indicates the formation of multiple layers of the conventional Fe/Zn phases (summarized in Table V) resulting from the reaction of solid iron with the liquid zinc bath. These layers were considerably thicker and had well-defined boundaries, as compared with the aforementioned 24-hour sample (Figure 4). Furthermore, the δ phase was composed of two distinct regions. One was coherent with the γ layer, while the other had the appearance of being permeated by capillaries terminating at the δ-adherent layer. A clear boundary between the δ-palisade and ζ phase was additionally found (Figure 5). As with the δ phase, the ζ phase also diverged into two regions. The first region was bonded with δ-palisade and possessed a dense structure without detailed tissues, while the other region appeared as "bamboo-type" rods, parallel to one another and perpendicular to the iron surface, as observed in Figure 5(b).
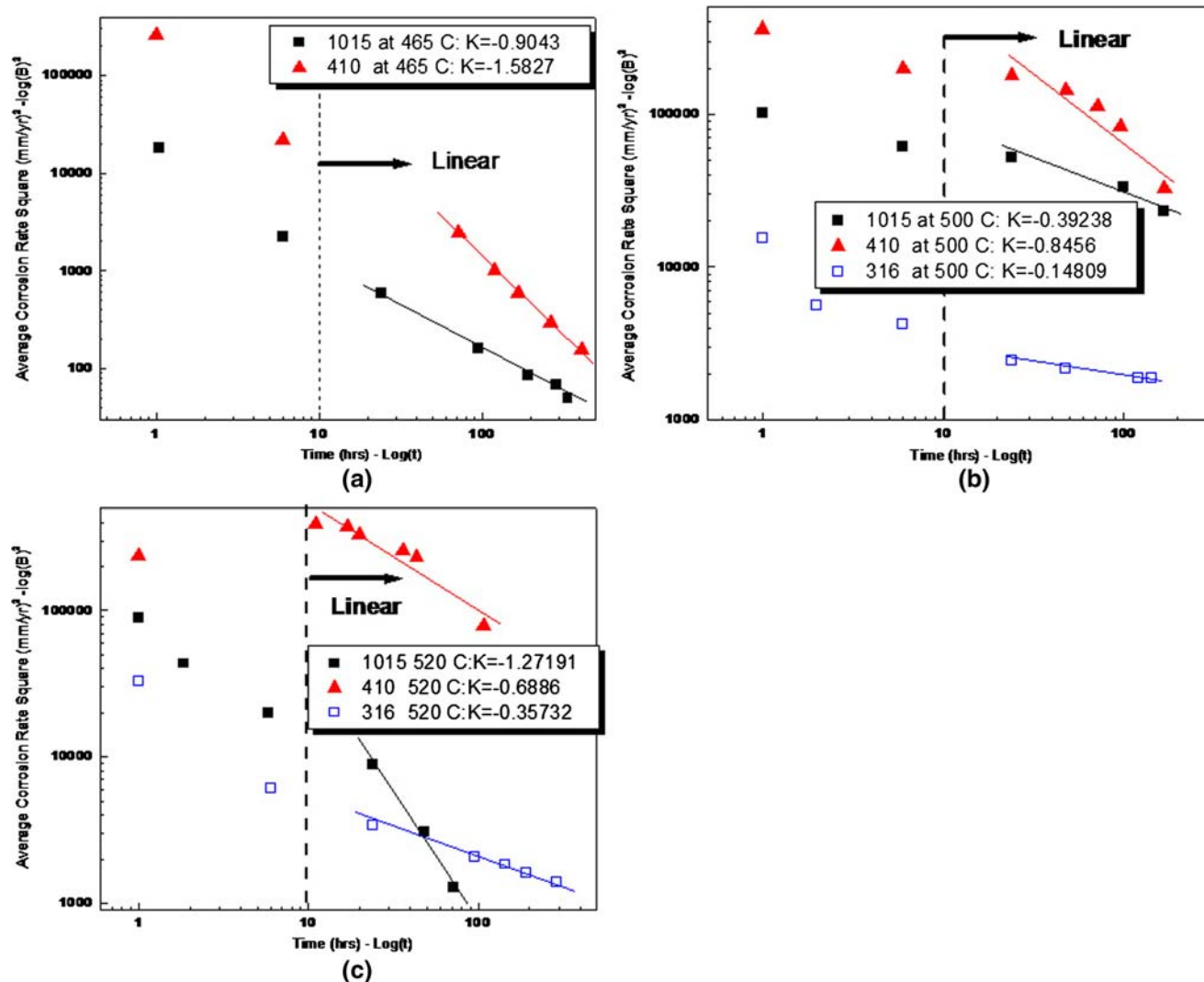
Fig. 3—Relationship between average corrosion rate square and time, log-log plot of 1015, 410, and 316L steels exposed to pure zinc at (*a*) 465 °C, (*b*) 500 °C, and (*c*) 520 °C.

Table IV. List of Corrosion Decaying Speed for Three Metals Exposed to Pure Zinc Bath

Corrosion Decay K (mm/y)^2/h	Bath Temperature (°C)		
	465	500	520
Steels			
1015 carbon steel	0.9043	0.3924	1.2719
410 stainless steel	1.5827	0.8456	0.6886
316L stainless steel	—	0.1481	0.3573

2. 316L stainless steel

As with the carbon steel samples, the 316L stainless steel microstructures also revealed the formation of typical Fe-Zn intermetallics, but were now impacted by the presence of chromium from the substrate metal. Figures 6 and 7 identify the cross-sectional microstructures on 316L stainless steel after immersing in molten Zn at 520 °C for 96 and 192 hours, respectively. Hence, after 96 hours (Figure 6), only a layer γ phase

($Fe_3Zn_{10}Cr_x$ [x = 2.5 to 3.5]) intermetallic was observed. However, as shown in Figure 7 and outlined in Table VI, when the immersion time was extended up to 192 hours, the intermetallic layers included not only γ phase but also δ phase ($FeZn_7Cr_x$ [x = 0.29 to 0.32]) through the following reaction:

$$L + \gamma \rightarrow \delta \qquad [3]$$
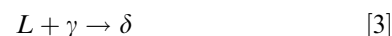
3. 410 stainless steel

Finally, even though 410 stainless steel possesses a considerable amount of chromium such as 316L stainless, the resultant corrosion morphologies more closely resembled the structures observed in the 1015 carbon steel samples. For example, looking at the 410 stainless steel sample, which was immersed in liquid zinc for 11 hours at 520 °C (Figure 8(a)), a clear interface between the steel and solidified zinc was found, analogous to the 24-hour carbon steel immersion sample.
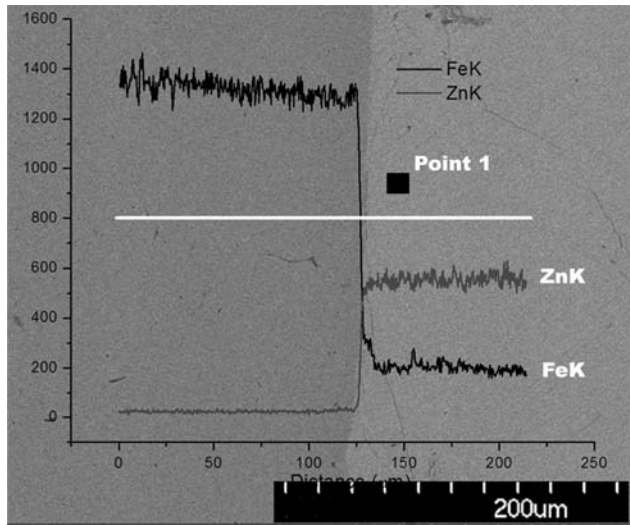
Fig. 4—Elements cross-sectional EDX profile of 1015 carbon steel dipping 24 h at 520 °C in Zn: (*a*) elemental distribution (Fe, Zn) and (*b*) chemical composition of location 1.

From the stainless interface into the solidified zinc region, the iron level decreased tremendously in the first 20- to 30-μm affinity region, and then stabilized. Analysis of the affinity region (location 1) near the interface (Figure 8(b)) identifies the chemical composition representative of γ phase with a small amount of Cr.

After a longer immersion time of 264 hours (at 465 °C), the coating microstructure on the 410 stainless sample is again similar to 1015 carbon steel in that it also contained a thick multilayer structure resulting from the reaction of steel with the zinc bath (Table VII). These layers were orderly arranged but without well-defined boundaries. The γ phase interface layer was approximately 20-μm thick, and appeared like a porous honeycombed structure as a result of pitting, especially at the boundary with the stainless substrate. Next, the ζ phase was composed of two distinct regions. One was
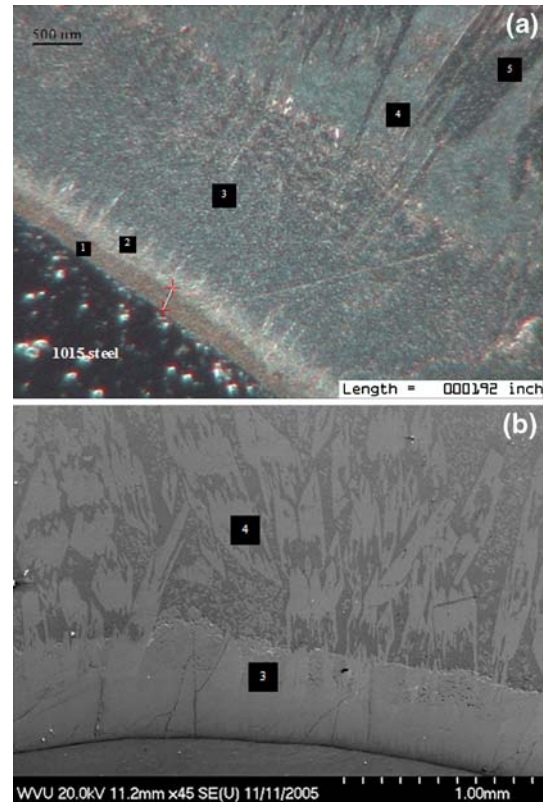

Fig. 5—Microstructure of 1015 carbon steel dipping 168 h at 500 °C in Zn bath. Layer 1 is γ phase Fe_3Zn_{10}; layer 2 is δ phase $FeZn_7$; layer 3 is ζ phase $FeZn_{13}$; layer 4 is ζ phase $FeZn_{13}$; and layer 5 is η phase Zn. Note: refer to Table V.

coherent with the γ layer bonded to the steel, while the other appeared as "bamboo-type" rods, parallel to one another and perpendicular to the iron surface (Figure 9(a)). Conversely, δ phase, which was observed on the 1015 steel sample, was not recognized on the 410 stainless. Finally, the elemental analysis indicated a decrease in the Cr concentration (from the Fe-Zn interface into the solidified zinc layer) from 4 at. pct in the γ phase to 1 at. pct in the ζ phase.

IV. DISCUSSION

A. *Comparison of the Corrosion Resistance of Various Steels*

Experimental data of the weight loss and corrosion rate clearly identified a ranking of the liquid zinc corrosion resistance for the three steels tested. Overall, 410 stainless steel exhibited the highest corrosion rate, while 1015 carbon steel had greater corrosion than 316L stainless steel. One exception to this generality was the

Table V. Phases Observed in the Residual Zinc Coating on the 1015 Carbon Steel Specimen after Immersion in Zinc at 500 °C for 168 Hours (Position 1 is the Interface between the Steel and Zinc; Position 5 Approaches the Outer Surface of the Zinc Coating)

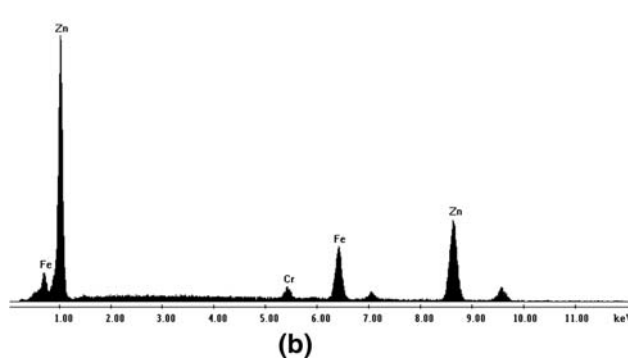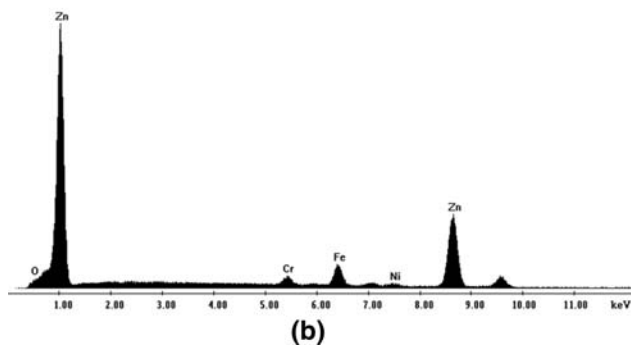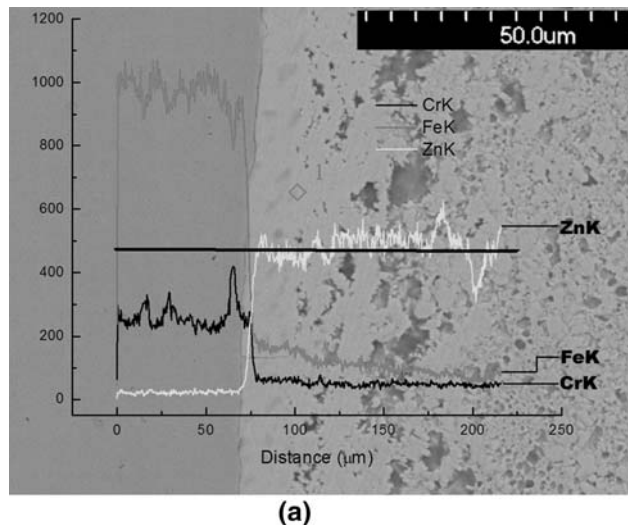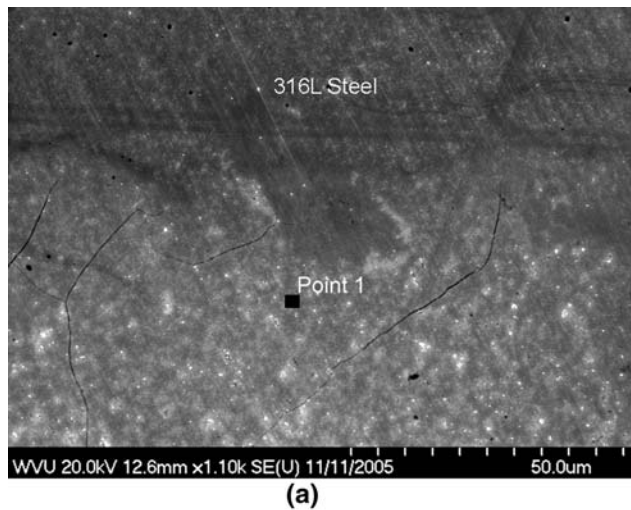| Position	Position 1	Position 2	Position 3	Position 4	Position 5
Compositional Phase	γ: Fe_3Zn_{10}	δ: $FeZn_7$	ζ: $FeZn_{13}$	ζ: $FeZn_{13}$	η: Zn

(a)

(b)

Fig. 6—Cross-sectional microstructure of 316 stainless steel dipping 96 h at 520 °C in Zn: (a) SEM and (b) EDX chemical composition of location 1.

(a)

(b)

Fig. 8—Cross-sectional EDX profile of 410 stainless steel after 11 h at 520 °C in Zn: (a) elemental distribution (Fe, Zn, and Cr) and (b) chemical composition of location 1.
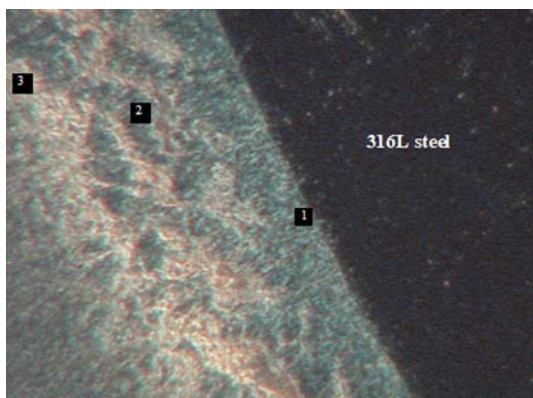

Fig. 7—Microstructure of 316 stainless steel dipping 192 h at 520 °C in Zn bath. Both layers 1 and 2 are γ-phase $Fe_3Zn_{10}Cr_x$, x = 2.5 to 3.5; layer 3 is δ phase $FeZn_7Cr_x$, x = 0.29 to 0.32. Note: refer to Table VI.

accelerated weight loss of 316L stainless steel (relative to 1015 carbon steel) for the time period between 48 and 96 hours. However, 316L experienced less cumulative degradation than 1015 carbon steel at 500 °C for the 180-hour testing duration, which was in accordance with previously documented conclusions based on experimental work at 480 °C for 120 hours.[4]

Earlier, it was postulated that corrosion resistance in liquid zinc is affected by not only the concentration of alloying elements (typically, Cr and Ni) in the substrate material but also the lattice structure of the metal. Comparing the tests results of 316L and 1015 reveals that the high alloying content (up to 18 pct Cr when working with 11 pct Ni) of 316L stainless performed better than unalloyed carbon steel. In addition, the face-centered cubic (fcc) structure in austenitic 316L is more compact than the body-centered-cubic (bcc) structure in ferritic 1015, providing theoretically slower diffusion and corrosion.

Table VI. Phases Observed in the Residual Zinc Coating on the 316l Stainless Steel Specimen after Immersion in Zinc at 520 °C for 192 Hours (Position 1 is the Interface between the Steel and Zinc)

Position	Position 1	Position 2	Position 3
Compositional Phase	γ: $Fe_3Zn_{10}Cr_x$, x = 2.5 to 3.5	γ: $Fe_3Zn_{10}Cr_x$, x = 2.5 to 3.5	δ: $FeZn_7Cr_x$, x = 0.29 to 0.32

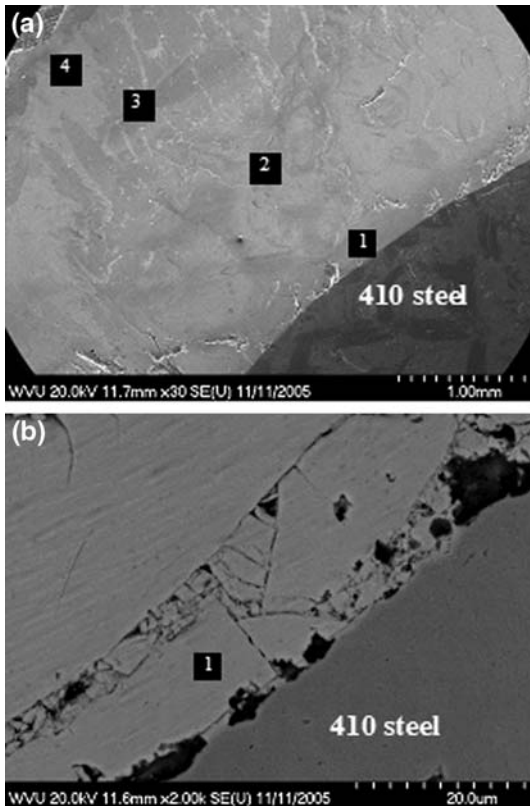| Position	Position 1	Positions 2 and 3	Position 4
Compositional Phase	γ: $Fe_3Zn_{10}Cr_x$, $x = 0.48$ to 0.50	ζ: $FeZn_{13}Cr_x$, $x = 0.065$ to 0.082	η: Zn

Fig. 9—Microstructure of 410 stainless steel dipping 264 h at 465 °C in Zn bath: (*a*) multilayer structure and (*b*) honeycombed structure from pitting. Layer 1 is γ phase $Fe_3Zn_{10}Cr_x$, $x = 0.48$ to 0.50; layer 2 is ζ phase $FeZn_{13}Cr_x$, $x = 0.065$ to 0.082; layer 3 is also δ phase $FeZn_7Cr_x$, $x = 0.29$ to 0.32; and layer 4 is η-phase Zn. Note: refer to VII.

However, the comparison between 1015 and 410 shows that the corrosion resistance of 410 in molten zinc is worse than that of 1015, even with the presence of 12 pct Cr in 410 steel. It is believed that this difference in corrosion is due to the dissimilar lattice structures between martensitic 410 steel and ferritic 1015 steel. The higher strain energy stored in a martensite structure potentially makes it more susceptible to corrosion with a higher lattice diffusion coefficient.[20] This finding is also supported by published corrosion tests of martensitic steel in water at 588 K, where specimens with wholly or partially martensitic structures were shown to corrode rapidly. The high corrosion rates are ascribed to high phase-transformation microstrains associated with the presence of the martensitic structure.[21,22]

B. Corrosion Mechanisms

The Fe-Zn system contains numerous phases including liquid zinc (η), intermetallic phases (γ_1, γ, δ, ζ), and terminal solid solutions of α-iron (bcc), γ-iron (fcc), and zinc (hcp). The γ_1 phase forms through the following peritectoid reaction at 550 °C.[9]

$$\gamma + \delta \rightarrow \gamma_1 \qquad [4]$$

However, because the testing temperatures in this article were 465 °C, 500 °C, and 520 °C, the γ_1 phase was not formed, which was subsequently confirmed by the SEM observation. As shown in Figure 10, the Fe-Zn binary phase diagram indicates that the magnetic ordering leads to a significant reduction of zinc solubility in α-iron.[23] The iron solubility in zinc is very low, typically, 0.00002 to 0.00007 wt pct at 419 °C, 0.029 to 0.030 wt pct at 450 °C, and 0.038 wt pct at 460 °C.

Dissolution mechanisms on steel by liquid zinc have been studied previously by several investigators,[18,24] who have determined that the diffusion coefficient of zinc is greater than that for steel ($D_{Zn} > D_{Fe}$).[25,26] Hence, it is widely believed that zinc readily diffuses into the steel and forms intermetallic compounds. Ghuman et al.[24] concluded that fully developed layers of conventional Fe-Zn phases, γ, δ, and ξ, resulted from the reaction of solid iron with the liquid zinc bath for short immersion times, but it is generally agreed that the intermetallic layers formed undergo progressive spallation and dissolution[18] after continued exposure. In support of these previous findings, the transformation of the kinetic process may be described herein using the semi-instant corrosion rate trend for the experimental data from 410 stainless steel immersed at 500 °C as an example (Figure 11). Based on further analysis of these data, the transformation may be depicted.

Step 1: Fe rapidly dissolves into zinc bath.
Step 2: The intermetallic layer on the surface of the steel specimen forms, suppressing the swift dissolution of Fe into the bath. This intermetallic phase at the iron surface impedes the opposite diffusion reaction between the iron and zinc. Because $D_{Zn} > D_{Fe}$ (diffusion coefficients) in the reaction layer, the interface moves deeper into the iron substrate forming a thicker intermetallic phase over time.

Meanwhile, portions of the intermetallic layer break down and spall from the surface, allowing the fresh iron surface to be exposed. Diffusing zinc atoms then react with the exposed iron and initiate additional growth of the conventional Fe-Zn phases. The iterative intermetallic formation and spallation eventually result in a cumulative weight loss of the substrate material.

Step 3: Once the intermetallic formation rate is balanced by the spallation rate (usually within the first 24 hours after immersion), the semi-instant corrosion rate stabilizes and the intermetallic layers grow
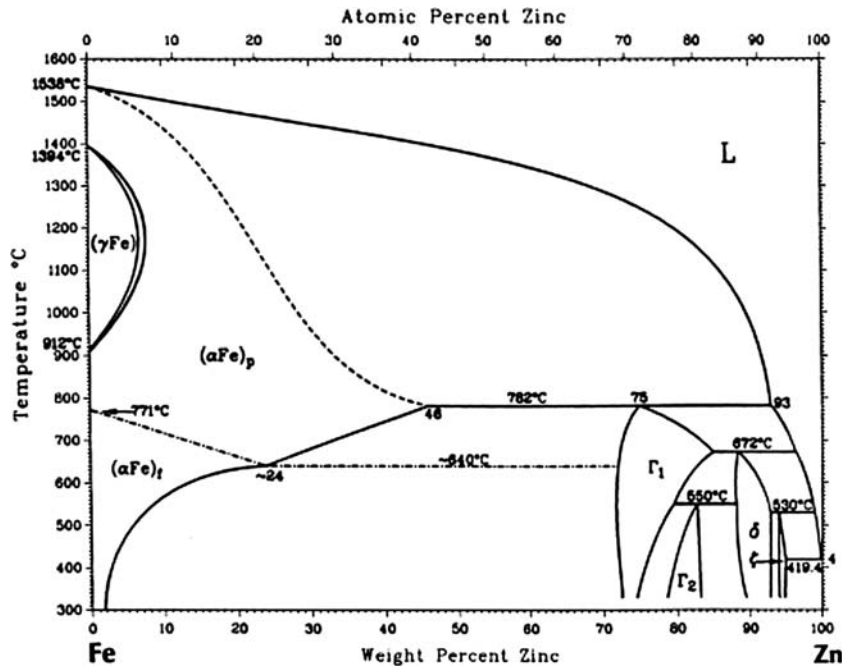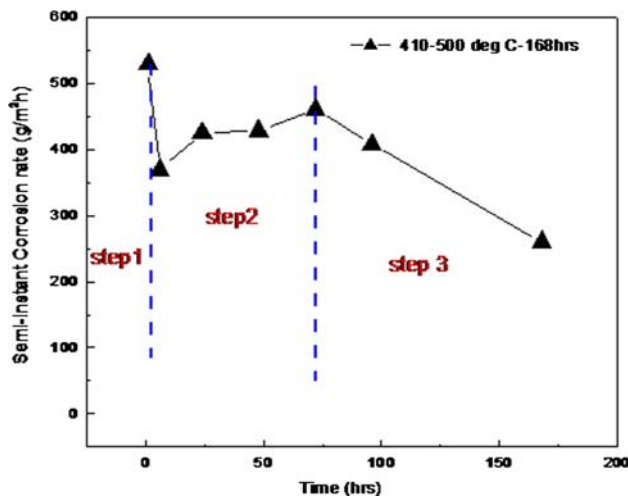
Fig. 10—Fe-Zn binary phase diagram.[20]

Fig. 11—Semi-instant corrosion speed of 410 stainless steel exposed to pure zinc at 500 °C.

rate of the interfacial reaction, and, thus, the intermetallic layer growth is controlled by zinc atoms passing through the interfacial layer, driven by the concentration gradient. Furthermore, at first glance, it seems puzzling that the weight loss plot (Figure 1) reflects exactly the linear-rate law, but it should be noted that the weight loss was the overall result of the surface area degradation and thickness reduction. Similarly, the average corrosion rate was based on the specimen thickness decrease, which was measured/calculated from the assumption that the surface area did not change. Alternatively, in order to account for the surface area changing during the experiments, the corrosion kinetics was described by the semi-instant corrosion rate (Figure 11), which had not only a linear substage representing the influence of interfacial reaction, but also a parabolic regime indicating the subsequent diffusion dominance.

V. CONCLUSIONS

Liquid metal corrosion of 316L stainless, 410 stainless, and 1015 carbon steel was studied through static corrosion tests in a molten zinc bath for various temperatures and times, and, as a result, several conclusions can be drawn from this investigation.

1. Under the experimental conditions in this article, 316L showed the best dissolution resistance to liquid zinc among these three alloys, while 1015 carbon steel had a lower solubility than 410 stainless.
2. Both composition and lattice structure played important roles in the molten metal corrosion behaviors of these alloys. High contents of Cr combined with Ni improved the resistance to molten

thicker. This enhancement of the intermetallic layers hinders the penetration of zinc, limiting its interaction with the iron substrate. Confirmed by the standard parabolic rule (Figure 3), the corrosion data indicate that this stage was diffusion controlled.

It has been shown in the literature that the corrosion kinetics of steels (1.4914 martensitic steel and 316L austenitic steel) exposed to liquid gallium at 400 °C also satisfied the parabolic regime for extended immersion times (e.g., greater than 40 hours[14]).

The parabolic law indicates that the corrosion process is controlled by diffusion after the first three stages for 24 hours. Hence, the rate of diffusion is slower than the

zinc corrosion. Meanwhile, an fcc structure indicated better corrosion resistance in the tested context than either bcc or body-centered-tetragonal (bct) due to the compact structure present in fcc materials. It appeared that the bct martensite lattice structure was more susceptible to corrosion possibly due to its wide atomic spacing (*i.e.*, noncompact structure) and high strain energy.

3. Bath temperature played an important role in both dissolution and intermetallic layer formation. Increasing the bath temperature accelerated the corrosion process and changed the nature of intermetallic layers.

REFERENCES

1. M. Brunnock, R. Jones, G. Jenkins, and D. Llewellyn: *Ironmaking and Steelmaking*, 1996, vol. 23, pp. 171–76.
2. X. Liu, E. Barbero, J. Xu, M. Burris, K.-M. Chang, and V. Sikka: *Metall. Mater. Trans. A*, 2005, vol. 36A, pp. 2049–58.
3. F. Goodwin, K.-M. Chang, and V. Sikka: *94th Annual Meeting*, Galvanizer's Association, Dearborn, MI, 2002.
4. M. Brunnock, R. Jones, G. Jenkins, and D. Llewellyn: *Zinc-Based Steel Coating Systems*, TMS, Warrendale, PA, 1998, pp. 51–62.
5. K. Tani and T. Tomita: *ISIJ*, 1994, vol. 34, pp. 822–28.
6. B. Seong, S. Hwang, M.C. Kim, and K.Y. Kim: *Surf. Coat. Technol.*, 2001, vol. 138, pp. 101–10.
7. M. Brunnock, R. Jones, G. Jenkins, and D. Llewellyn: *Ironmaking and Steelmaking*, 1997, vol. 24, pp. 40–46.
8. E. Barbero, X. Liu, B. Kang, J. Loth, J. Snider, V. Sikka, and F. Goodwin: *95th Annual Meeting*, Galvanizer's Association, Monterrey, Mexico, 2003.
9. N. Tang: *J. Phase Equilib.*,, 2000, vol. 21 (1), pp. 70–77.
10. X. Su, N. Tang, and J.M. Toguri: *J. Alloys Compd.*, 2001, vol. 325, pp. 129–36.
11. N. Tang, Y. Liu, and K. Zhang: *44th Mechanical Working and Steel Processing Conf. Proc. (Iron and Steel Society)*, 2002, vol. 40, pp. 815–21.
12. N. Tang: *97th Annual Meeting*, Galvanizer's Association, Lexington, KY, 2005.
13. N. Tang: *ZCO-15-4: Dross Buildup–Influences on the Hardware Materials and Line Operating Conditions*, ILZRO Progress Report, International Lead Zinc Research Organization, Research Triangle, NC, Oct. 2005.
14. E. Pennell:: *76th Annual Meeting*, Galvanizer's Association, West Middlesex, PA, 1984.
15. B. Dugan: AGA Galvanizing Note, American Galvanizers Association, Centennial, CO, Mar. 2006.
16. M. Bright: Ph.D. Dissertation, West Virginia University, Morgantown, WV, 2007.
17. V. Dybkov: *J. Mater. Sci*, 1990, vol. 25, pp. 3615–33.
18. F. Barbier and J. Blanc: *J. Mater. Res*, 1999, vol. 14, pp. 737–44.
19. D. Hortsmann and F.K. Peters: *Proc. Conf. Intergalva '70*, Industrial Newspaper Ltd., London, UK, 1970, pp. 75–105.
20. A. Turnbull and M.W. Carroll: *Corr. Sci.*, 1990, vol. 30, pp. 667–79.
21. R.A. Holt and F.G. Elder: AECL-4586, Jan. 1974, 12 pp.
22. K. Hidehiko and S. Hideo: *Corr. Eng.*, 1985, vol. 34, pp. 18–22.
23. *ASM Handbook*, vol. 3, *Alloy Phase Diagrams*, ASM INTERNATIONAL, Materials Park, OH, 1992.
24. A.R.P. Ghuman and J.I. Goldstein: *Metall. Trans.*, 1971, vol. 2, pp. 2903–14.
25. A. Allen and J. Mackowiak: *J. Inst. Met.*, 1962–63, vol. 91, pp. 369–72.
26. M. Andreani, P. Azou, and P. Bastien: *C.R. Acad. Sci. Paris*, 1966, vol. 263, pp. 1041–43.